

# Single Particle Detection System for Strong-Field QED Experiments

F C Salgado<sup>1,2</sup>, N Cavanagh<sup>3</sup>, M Tamburini<sup>4</sup>, D W Storey<sup>5</sup>,  
R Beyer<sup>6</sup>, P H Bucksbaum<sup>7</sup>, Z Chen<sup>5</sup>, A Di Piazza<sup>4</sup>,  
E Gerstmayr<sup>7</sup>, Harsh<sup>1,2</sup>, E Isele<sup>7</sup>, A R Junghans<sup>6</sup>, C Keitel<sup>4</sup>,  
S Kuschel<sup>5,8</sup>, C F Nielsen<sup>9</sup>, D A Reis<sup>7</sup>, C Roedel<sup>10</sup>, G Sarri<sup>3</sup>,  
A Seidel<sup>1,2</sup>, C Schneider<sup>6</sup>, U I Uggerhøj<sup>9</sup>, J Wulff<sup>1,2</sup>,  
V Yakimenko<sup>5</sup>, C Zepf<sup>1,2</sup>, S Meuren<sup>7</sup>, and M Zepf<sup>1,2</sup>

<sup>1</sup> Institut für Optik und Quantenelektronik, Friedrich-Schiller-Universität Jena, Max-Wien-Platz 1, 07743 Jena, Germany

<sup>2</sup> Helmholtz-Institut Jena, Fröbelstieg 3, 07743 Jena, Germany

<sup>3</sup> Queen's University Belfast, University Road, BT7 1NN Belfast, United Kingdom

<sup>4</sup> Max-Planck-Institut für Kernphysik, Saupfercheckweg 1, D-69117 Heidelberg, Germany

<sup>5</sup> SLAC National Accelerator Laboratory, Menlo Park, California 94025, USA

<sup>6</sup> Institute for Radiation Physics, Helmholtz-Zentrum Dresden-Rossendorf, Germany

<sup>7</sup> Stanford PULSE Institute, SLAC National Accelerator Laboratory, Menlo Park, California 94025, USA

<sup>8</sup> Institut für Experimentalphysik, University of Hamburg, Germany

<sup>9</sup> Department of Physics and Astronomy, Aarhus University, 8000 Aarhus, Denmark

<sup>10</sup> Institute of Nuclear Physics, Technical University Darmstadt, Schlossgartenstr. 9, 64289 Darmstadt, Germany

E-mail: felipe.salgado@uni-jena.de

June 2021

**Abstract.** Measuring signatures of strong-field quantum electrodynamics (SF-QED) processes in an intense laser field is an experimental challenge: it requires detectors to be highly sensitive to single electrons and positrons in the presence of the typically very strong x-ray and  $\gamma$ -photon background levels. In this paper, we describe a particle detector capable of diagnosing single leptons from SF-QED interactions and discuss the background level simulations for the upcoming Experiment-320 at FACET-II (SLAC National Accelerator Laboratory). The single particle detection system described here combines pixelated scintillation LYSO screens and a Cherenkov calorimeter. We detail the performance of the system using simulations and a calibration of the Cherenkov detector at the ELBE accelerator. Single 3 GeV leptons are expected to produce approximately 300 detectable photons in a single calorimeter channel. This signal is compared to Monte-Carlo simulations of the experiment. A signal-to-noise ratio of 32 in a single Cherenkov calorimeter detector is expected and a spectral resolution of 2% is achieved using the pixelated LYSO screens.

*Keywords:* strong-field QED, pair-creation, single-particle detection, Cherenkov calorimeter, Breit-Wheeler process Submitted to: *New J. Phys.*

## 1. Introduction

The interaction between light and matter is described by the theoretical framework of quantum electrodynamics (QED). In the perturbative limit, it is considered to be the most precise and well-tested theory of modern physics [1]. As the electric field strength approaches the so-called Schwinger critical field  $E_s \approx 1.3 \times 10^{18}$  V/m, novel strong-field quantum effects become important. Consequently, the description of electron-laser interactions must be described by dressed states as  $a_0 \gg 1$  and by high-order processes with radiative corrections scaling with  $\alpha\chi_e^{2/3}$  included in the theory [2], which is referred to as strong-field QED (SF-QED), where  $\alpha$  is the fine-structure constant.

The normalized vector potential  $a_0$  is a Lorentz invariant given, in Heaviside-Lorentz natural units ( $c = \hbar = \epsilon_0 = 1$ ), by  $a_0 = eE/(m_e\omega_0)$ . Here,  $e$  is the absolute electron charge,  $E$  the peak value of the laser electric field and  $m_e$  is the rest mass of the electron [2]. Another important parameter in the theory of SF-QED is the quantum parameter  $\chi_e$ . It is defined, also in natural units, as  $\chi_e = a_0\gamma_e(\omega_0/m_e)(1 - \cos\theta)$ , where  $\gamma_e$  is the colliding electron beam Lorentz-factor,  $\omega_0$  is the laser frequency, and  $\theta$  is the collision angle between the electron with the laser beam (for head-on collision  $\theta = 180^\circ$ ). A parameter  $\chi_e \gtrsim 1$  indicates that high-energy photon emission by the electron is likely, and, therefore, the particle undergoes a significant recoil on its motion.

Fundamental processes involving photon emission and photon decay are modified under strong-fields and mechanisms such as multi-photon Compton scattering, radiation reaction and nonlinear Breit-Wheeler (BW) are examples of predictions resulting from SF-QED. However, the experimental investigation of this regime is very limited to date [3]. Few experiments utilize the high-intensity fields in collisions of ultra-relativistic ions [4] or the interaction of ultra-relativistic particles in aligned crystals [5]. Recently, the investigation of SF-QED has been proposed using the collision of tightly focused ultra-relativistic electron beams [6].

With the advent of ultra-intense laser pulses [7, 8], strong electric fields can be achieved in the laboratory by strongly focusing ultra-intense lasers. However, the Schwinger critical field is still far beyond the reach of present laser technology by around 3-4 orders of magnitude [9]. A solution for this challenge is to combine the highest achievable electric field from laser pulses with ultra-relativistic electron beams or  $\gamma$ -photons, allowing the Schwinger field to be achieved in the rest frame of the electrons. In addition to pair generation, the vacuum responds nonlinearly and processes such as light-light scattering [10] and vacuum birefringence [11] can occur and be detected [12]. A review of strong-field QED processes is found in Ref. [3].

The first experiments in the strong-field QED processes using intense laser fields and ultra-relativistic electron beams were reported in the Experiment-144 at SLAC in the 1990s [13–15]. In this experiment, electron bunches were accelerated by a linear accelerator up to energies of 49.1 GeV and interacted with a laser field with a root mean square (RMS) normalized vector potential of  $a_0^{RMS} = 0.4$  and  $\chi_e^{RMS} \approx 0.3$  producing about 100 positrons in total in the perturbative multi-photon regime ( $\chi_e < 1$  and

$a_0 < 1$ ) [13–15].

Experiments have been proposed for investigating SF-QED effects based on the interaction of high energy electron or photons beams with high-intensity lasers or nuclear fields in crystals [5, 16]. Moreover, experiments investigating pair production, multi-photon Compton scattering and radiation reaction using all-optical setups have been proposed and realised at the Astra-Gemini laser system at the Rutherford Appleton Laboratory (RAL) [17–19]. In such experiments, electron beams generated by laser-wakefield acceleration (LWFA) up to 2 GeV interacted with an intense laser pulse with  $a_0 = 10$  [18, 19] at the nonperturbative moderate quantum regime ( $\chi_e < 1$  and  $a_0 > 1$ ), and signatures of radiation reaction process were observed. Upcoming projects aim to investigate SF-QED effects in the nonperturbative full quantum regime, i.e.  $\chi_e > 1$  and  $a_0 > 1$ . Interactions can be between two beams of photons [10] or between electron beams and intense laser pulses as proposed in the Experiment-320 (E-320) at FACET-II [20–22] and the LUXE experiment at DESY [23–25]. In both experiments, a small number of electron-positron pairs, which are generated by SF-QED processes must be measured with a sensitive detection system. The challenge in the detector development is that the detection system must be able to detect single particles, while also being insensitive to the photon background which is inherent to the experiments with an ultra-relativistic electron beam and a beam dump close to the interaction region.

In Figure 1, the different regimes of interaction of each SF-QED experiment with electron-laser interaction are highlighted.

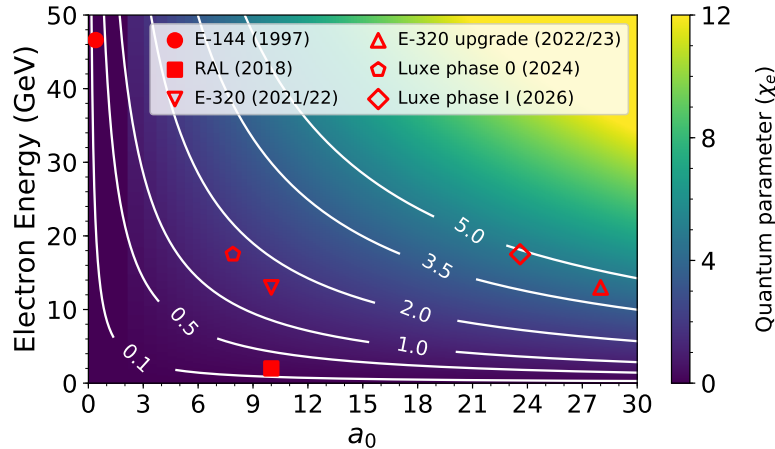


**Figure 1.** Electron quantum parameter  $\chi_e$  for different normalized laser strength  $a_0$  and incoming electron energies. The filled red markers indicates the already performed experiments: (circle) Experiment-144 (E-144), 1997 [13, 14]; (square) RAL, 2018 [19]. The open markers shows the upcoming SF-QED experiments: (up-pointing triangle) Experiment-320 (E-320), 2021/2022 [20]; (down-pointing triangle) Experiment-320 upgrade, 2022/2023 [20]; (pentagon) LUXE phase 0, 2024 [25]; (diamond) LUXE phase 1, 2026 [25]. The Experiment-320 will probe the nonperturbative full quantum regime of interaction ( $\chi_e > 1$  and  $a_0 > 1$ ).

Here we describe the detection system which is designed for SF-QED experiments such as the E-320 at FACET. We report a detection system which is able to diagnose single particles with MeV to GeV energies. A test and calibration of the detector system is presented. Monte-Carlo simulations of the background noise level and the expected signal-to-noise ratio for the E-320 show that single positron events can be detected with an expected signal-to-noise ratio of 32.

## 2. Single Particle Detection System

The detection system comprises two pixelated LYSO:Ce crystal screens to provide high spatial resolution coupled to a segmented Cherenkov calorimeter both placed about 3.6 m after a dipole magnet. The screens are placed in front of a Cherenkov calorimeter, and thus provides the ability to discriminate against low energy background events. Both detectors have fast (nanosecond-scale) response which allows timing-based background suppression as well. Figure 2 presents the setup of the single particle detection system.

The two LYSO screens have crystal pixels with dimensions  $2\text{ mm} \times 2\text{ mm} \times 4\text{ mm}$  which provide tracking information on the single particles propagating towards the detector. In addition, The LYSO:Ce crystal has a decay time of about 40 ns which allows the background noise from secondary sources of radiation located far from the detectors to be suppressed by imaging the screens using gated ICCD cameras [26].

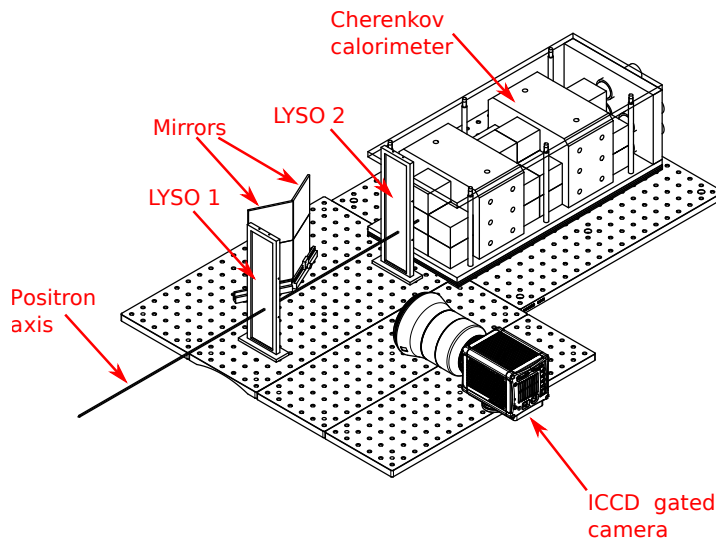


**Figure 2.** Proposed design of the single particle detection system for E-320 at FACET-II. The incident single GeV-positron travels through two pixelated LYSO scintillating screens which provides particle tracking and high resolution spectral information before entering the Cherenkov detector at one of its lead-glass detection channels where its energy is fully deposited. The Cherenkov photons produced inside the lead-glass channel are detected by photomultiplier tubes at the rear of each channel.

The Cherenkov calorimeter, which is placed behind the pixelated LYSO screens, comprises up to 7 detection channels of  $50\text{ mm} \times 40\text{ mm} \times 400\text{ mm}$  Schott F2 lead-

glass wrapped in enhanced specular reflector (ESR) foils to prevent the optical photon cross-talk between the detection channels. The F2 lead-glass has a radiation length of  $X_0 = 3.14\text{ cm}$  and a Mòliere radius of  $R_M = 3.4\text{ cm}$ . Hence, the glass blocks of the Cherenkov calorimeter were designed to contain the particle shower produced by a single  $3\text{ GeV}$  positron incident on it as shown in Figure 3. The calorimeter array consists of up to 7 blocks with the positrons designed to be incident on the the 3 central channels and positioned to detect positrons initially in the  $2.5 - 5.6\text{ GeV}$  range for a nominal  $87.2\text{ MeV}$  transverse kick of the dipole magnet. However, the kick settings of the dipole magnet are possible to be selected for detection of particles at alternative energy ranges. The side channels provide on shot background reference to allow better discrimination of signal events. Detection of the Cherenkov photons is achieved with photomultiplier tubes (PMTs) placed at the rear of each detection channel [27]. The PMTs used on the detector have a rise time of about  $3\text{ ns}$  therefore also allowing background noise rejection by temporal gating.

### 2.1. Calibration of the Cherenkov Calorimeter

The Cherenkov calorimeter was calibrated at the ELBE radiation source at the Helmholtz-Zentrum Dresden-Rossendorf (HZDR) using the dark current of the accelerator, which provides single electrons with  $27\text{ MeV}$  energy with a mean number of  $0.164$  electrons/RF cycle. The calibration of the ELBE accelerator dark current is presented in detail in Appendix A.

The dark current measurement was performed on the central calorimeter channel with the PMT gain set to  $4 \times 10^6$ , corresponding to a voltage across the cathode and anode of the PMT of  $10^3\text{ V}$ . The signals of the PMTs was recorded using PicoScopes [28]. A total of  $10^4$  events were acquired, and the number of Cherenkov photons detected by the PMTs as well as the signal decay time of each event are shown in Figure 4.

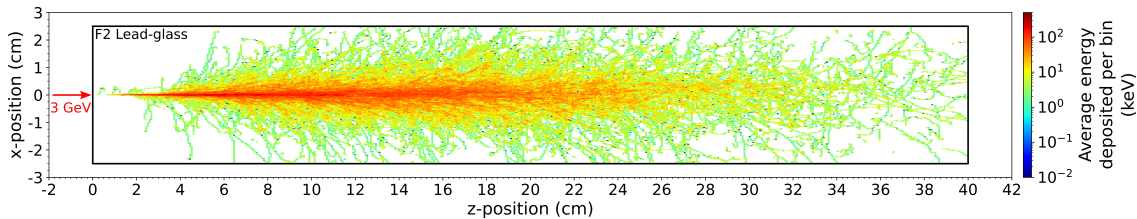


**Figure 3.** Simulated energy deposition for a single  $3\text{ GeV}$  positron inside a single F2 lead-glass block  $50\text{ mm} \times 40\text{ mm} \times 400\text{ mm}$  of the Cherenkov calorimeter. The lateral electromagnetic shower is well contained within the Mòliere radius ( $R_M = 3.4\text{ cm}$ ) inside a single calorimeter block. Each bin has an area of  $0.1\text{ mm}^2$ .

From Figure 4(a), an average of 4 photons are detected by the photomultiplier tube after a single electron with  $27\text{ MeV}$  energy hits the detection channel. From Monte-Carlo simulation using GEANT 4 [29–31], it is predicted that a single  $27\text{ MeV}$  electron produces 1770 photons. Therefore, the system has a photon detection efficiency

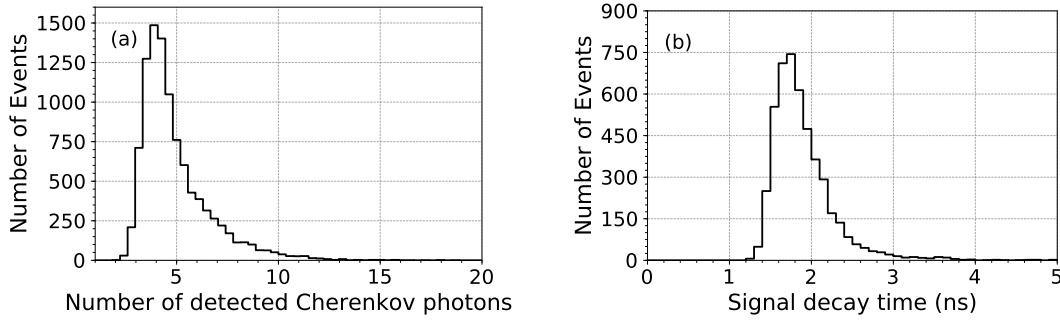


**Figure 4.** Cherenkov calorimeter calibration results using the single electrons obtained using the dark current of ELBE radiation source at the Helmholtz-Zentrum Dresden-Rossendorf (HZDR). The dark current of the linear accelerator is composed of single 27 MeV electrons. (a) Number of Cherenkov photons detected by the Cherenkov calorimeter - an average of 4 photons per single electron is detected; (b) decay time of the recorded signal - a single electron hit produces a signal which is about 1.8 ns long.

of 0.22 %. Together with the PMT detector efficiency of  $\approx 20\%$  we derive a photon transport efficiency in the calorimeter of  $\approx 1.2\%$ .

Based on this calibration and the scaling of Cherenkov photons derived from GEANT4 simulations we calculate the number of detected photons for different energies of incoming single particles, see Figure 5. Approximately 300 photons are detected for a single 3 GeV particle, providing an easily observed signal for single GeV-particle hits. The spectral resolution of the calorimeter is limited by statistical nature of the Cherenkov photon generation in the shower to approximately 20 %. Higher spectral resolution is provided by the LYSO screens in combination with the Cherenkov detectors for event rejection as discussed in the following section.

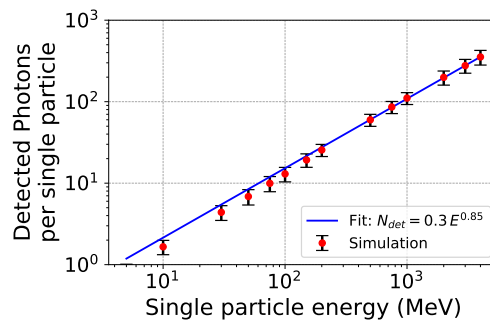


**Figure 5.** Calculated number of Cherenkov photons detected per channel for a single incident particle of different energies after the detection efficiency of 0.22 % is taken into account. The error-bars indicate the standard deviation which determine the energy resolution of the calorimeter. A single 3 GeV particle results in 300 detected photons by the calorimeter Hence, a single GeV-particle incident on the detector is easily detected by the calorimeter.

### 3. Proposed Implementation for the Experiment-320: Expected Performance

In this section, we present the experimental parameters of the Experiment-320 followed by a discussion of the background noise and the signal-to-noise ratio expected on the single particle detection system.

The E-320 uses the FACET-II linear accelerator to generate electron beams up to 13 GeV and a charge of 2 nC [32]. Only 1% of the electron bunch spatially overlaps with the focused laser pulse and interacts with a peak intensity of  $1.3 \times 10^{20} \text{ W/cm}^2$  which corresponds to an  $a_0 = 10$  and, consequently, a quantum parameter  $\chi_e = 1.5$  [20, 21] becomes experimentally accessible. As a result, E-320 will probe a regime where the interaction with the laser is nonperturbative and electron-positron pair-creation occurs in the tunneling regime [33].

The emission of high-energy photons in the strong laser field reduces the initial electron energy. Some of the high-energy emitted photons, while still immersed in the laser field, interact with the optical photons of the laser and generate electron-positron pairs through the nonlinear BW process. The created pairs propagate through the FACET-II spectrometer beamline alongside with the remains of the primary 13 GeV electron beam and the high energy photons, up to the dipole magnet where the charged particles are deflected towards the detectors and beam dump.

A slice of the FACET beamline with the positioning of devices such as the dipole magnet and the single particle detector is presented in Figure 6.

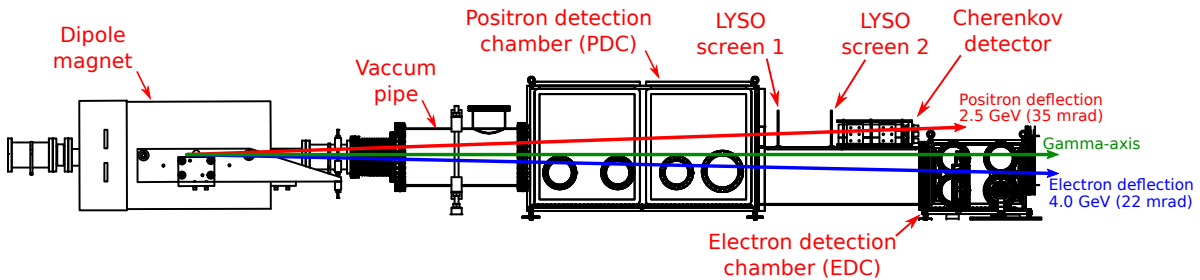


**Figure 6.** FACET-II beamline with the envisioned position of the single-particle detection system. The dipole magnet disperse the positrons upwards (red trajectory corresponds to a 2.5 GeV positron) where the single particle detection system is installed, and the electrons downwards (blue trajectory corresponds to a 4.0 GeV electron). The gamma beam is represented by the green trajectory.

The positrons are dispersed upwards by the dipole magnet and they travel through the positron detection chamber (PDC) before exiting through a 5 mm thick aluminum vacuum exit window to reach the LYSO pixelated screens, and, finally, the Cherenkov detector. On the other hand, electrons are dispersed downwards with particles deflected in the 22–65 mrad range being detectable by detectors in the electron detection chamber (EDC), while electrons deflected at angles greater than 65 mrad strike the chamber floor and beamline support structures and thus becoming a background source for the

detectors.

A beam dump is placed approximately 8.6 m downstream from the Cherenkov detector to stop the main electron beam and the produced high-energy photons. When the high-energy particles interact with the beam dump, substantial radiation in the backward direction that has the potential to reach the detectors and becomes noise is generated. However, the large distance between the detectors and the beam dump corresponds to a delay of 57 ns between a particle signal hit and the backscattered radiation on the detectors which is enough to significantly reduce dump noise at the detectors by time gating the PMTs and LYSO screens. Hence, the remaining background at the LYSO screens and detectors considered in the simulations below originates from the upstream radiation sources and secondary particles sources located very closely to the detectors which arrive within the gating window of the detectors.

#### 4. Background and Signal-to-Noise Ratio Estimates for the Experiment-320

To efficiently detect single particles with high confidence, the design goal for the Cherenkov detectors was to achieve a signal-to-noise ratio in terms of signal power to background power ( $\text{SNR}_P = P_S/P_{BG}$ ) approximately equal or greater than unity and a signal-to-noise ratio in terms of mean to variance ( $\text{SNR}_\sigma = \mu/\sigma \gg 1$ , where  $\mu$  and  $\sigma$  are mean value of signal and variance of the background respectively). This is particularly important for data taking at low signal rates, where the number of pairs to be detected per shot is  $\approx 1$  or less. Under these circumstances the Cherenkov detector allow the rejection of false positive events in the tracking detector and therefore the accumulation of tracking data to record high resolution spectra at low event rates.

Monte-Carlo simulations were performed using the code FLUKA [34, 35] for modelling the expected background noise at the positron detectors. In the simulations, only the electrons that actively contribute to the background noise generation were used. Hence, from the theoretical energy spectrum after the electron-laser interaction provided in Refs. [20, 21], just the  $10^7$  primary electrons in the energy range between 1 GeV to 12.8 GeV were included, while the unperturbed 13 GeV electrons were presumed to propagate to the dump and therefore be outside the gating window of the detectors.

Figure 7 presents the simulated particle fluence at the detection region, corresponding to the layout in Figure 6. Our simulations predict that the majority of background at the detectors arises from the secondary particles generated due to the interaction of low energy scattered electrons with the bottom of the vacuum chamber.

The particle spectrum of the background incident on the Cherenkov calorimeter is shown in Figure 8(a). As can be seen, the incoming background is mainly composed by photons with energy lower than 25 MeV. The number of Cherenkov photons produced inside a detection channel per incoming particle energy is presented in Figure 8(b). Summing up all Cherenkov photons generated we find a total of  $N_{BG} = 1.4 \times 10^5$  Cherenkov photons per primary electron bunch with a standard variation of  $\sigma = 4.2 \times 10^3$ . From Monte-Carlo simulations, a single 3 GeV positron (characteristic of

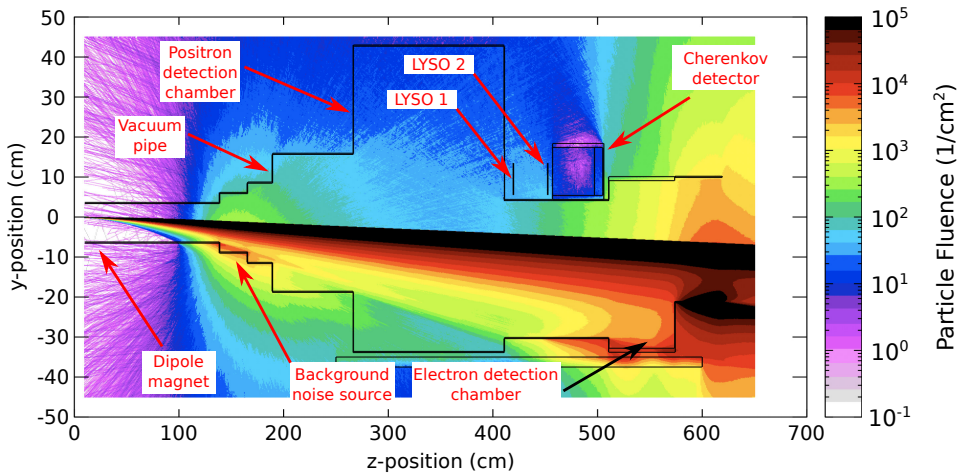


**Figure 7.** Expected particle fluence (gamma photons, electrons and positrons) at the FACET-II tunnel where the single particle detection system is installed. A shower of secondary particles from the interaction between the deflected primary electron beam with the chamber and vacuum pipe walls travels directly to the detectors generating background noise which cannot be gated.

expected positron energies) is expected to produce  $N_{SIG} = 1.34 \times 10^5$  Cherenkov photons inside a detection channel which corresponds to 300 detected photons after the transmission efficiency is taken into account (Section 2.1). The expected signal-to-noise ratio (SNR) in terms of detected photons is therefore  $SNR_P = N_{SIG}/N_{BG} = 0.95$  i.e. the number of optical photons within the detection channel is approximately doubled when a signal positron is present. The background signal irradiates the Cherenkov detector stack in a smoothly varying fashion. Since signal positrons are incident only on the central channels, the background reference calorimeter channels allow the background to be subtracted on every shot with a precision limited only by the variance of the background. The more important SNR measure is therefore the alternative definition of signal to background variance  $\sigma$ . This is predicted to be  $SNR_\sigma = N_{SIG}/\sigma \approx 32$ , demonstrating that individual positrons can clearly be separated from the background.

The higher spatial resolution of the LYSO crystals enables pair spectra to be measured with a resolution of 40 MeV at 2.5 GeV for nominal dipole magnet settings. Recording a spectrum at low count rates of  $< 1$  pair per shot requires integration of many shots and therefore efficient rejection of background events.

To this end, the energy deposited in each LYSO screen by a single particles hit was evaluated using Fluka as shown in Figure 9. A single 3 GeV positron deposits about 5.6 MeV on the first LYSO screen in an area only slightly larger than a pixel and 8.8 MeV in a cluster of pixels in the second scintillating screen. Most of the hits shown in Figure 10 on LYSO screen-1 and screen-2 can be rejected based on the above thresholds alone. Events that meet the energy threshold (example highlighted Figure 10) in both screens can be rejected by the calorimeter channels and allow high resolution spectra to be obtained from the LYSO screens, by integrating only those shots where

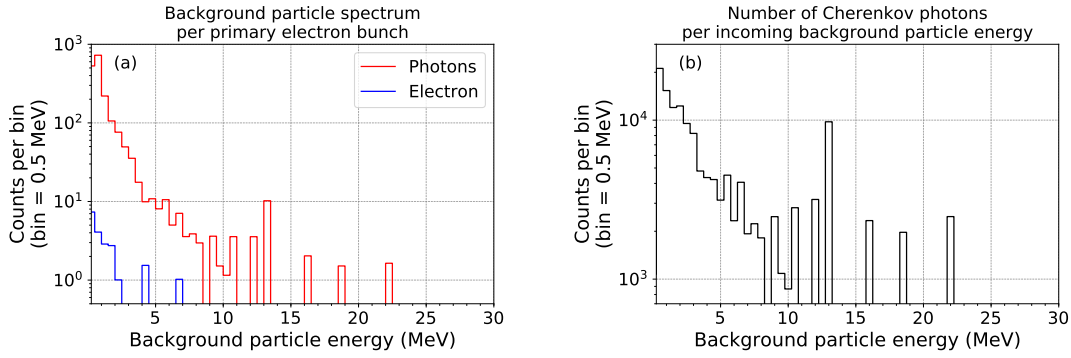


**Figure 8.** Background spectrum at a single Cherenkov calorimeter detection channel at the Experiment-320: (a) Background noise particle spectrum, most of the noise have energies below 25 MeV; (b) Number of Cherenkov photons produced per energy of incoming background particle, a total of  $1.4 \times 10^5$  photons is produced inside a single Cherenkov calorimeter channel.

the combination of detectors leads to the identification of  $> \text{GeV}$  positron.

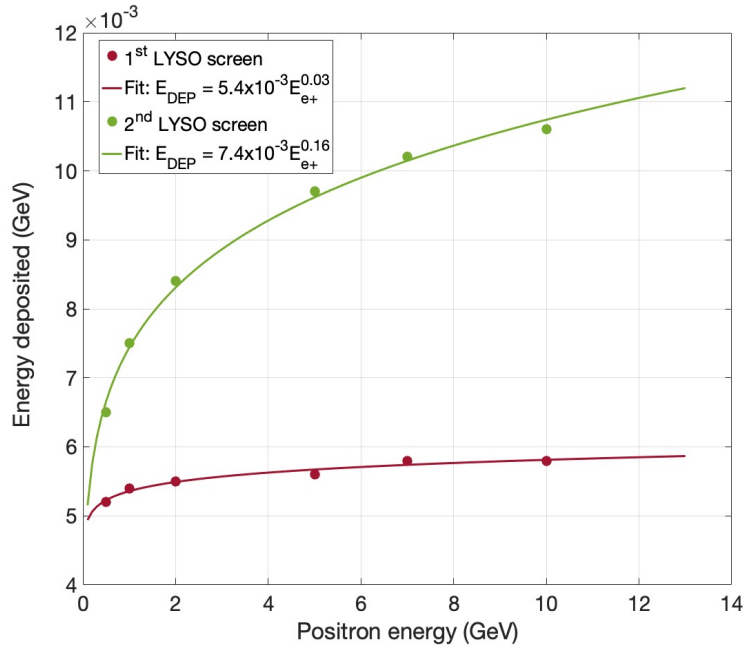


**Figure 9.** Energy deposited at each LYSO scintillating screen per incoming single particle with error bars indicating a standard deviation. As the incoming particle travels through the first crystal screen, secondary particles with lower energy are created increasing the energy deposited at the second screen in comparison with the first LYSO. The typical uncertainty on the data points is on the order of 3-5%.

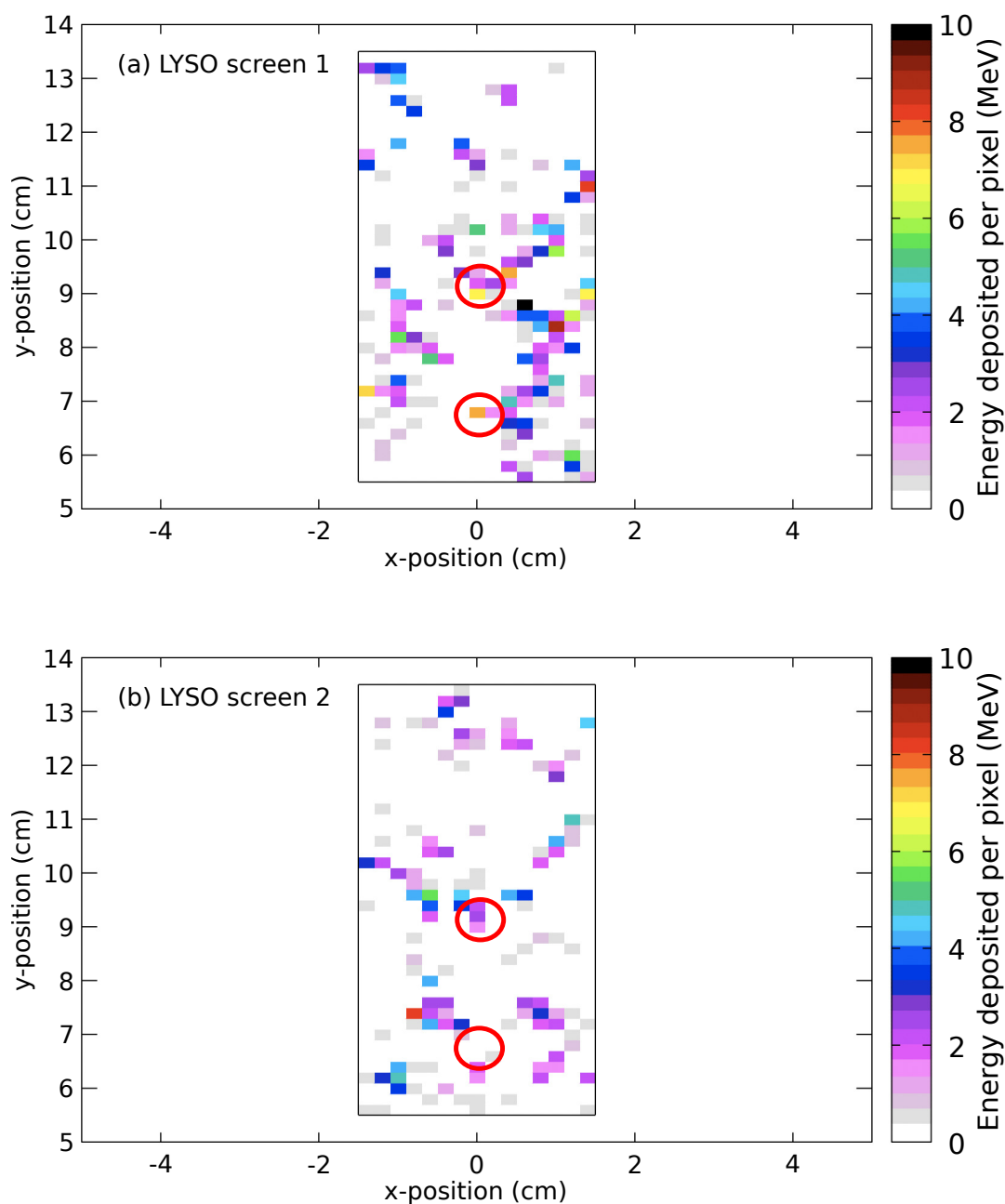


**Figure 10.** Energy deposited at the LYSO screens at the Experiment-320: (a) LYSO screen 1; (b) LYSO screen number 2. All background events (with exception of event highlighted by a red circle) on screen-1 can be rejected due to energy deposited per pixel on screen-1 or absence of  $> 6$  MeV pixel cluster on screen-2. The highlighted pixel in the centre of screen-1 and area on screen-2 would be consistent with a  $> 1$  GeV incident positron, but can be rejected due to the calorimeter signal.

## 5. Conclusions

In this paper, a single particle detection system designed to measure positron spectra for strong-field QED experiments is presented. The implementation in the upcoming Experiment-320 at FACET-II (SLAC) is detailed with calibration data from the ELBE accelerator. Based on this calibration a single 3 GeV particle hit at the Cherenkov detector generates about 300 detectable photons by the calorimeter with an energy resolution of  $\approx 20\%$ . Furthermore, Monte-Carlo simulations were performed to demonstrate that a signal-to-noise ratio of  $\text{SNR}_\sigma = 32$  is predicted for the Cherenkov calorimeter detector at the Experiment-320. The combination of the LYSO screens with the Cherenkov detector allows efficient rejection of background events and the recording of positron spectra with  $\Delta E/E = 0.02$  even for pair production rates of  $\ll 1$  per shot.

## Acknowledgments

This research work was funded by DFG Research Group 2783 "Quantumvacuum". Parts of this research were carried out at ELBE at the Helmholtz-Zentrum Dresden - Rossendorf e. V., a member of the Helmholtz Association. We would like to thank the ELBE and FACET staff for their assistance. This work was supported by the U.S. Department of Energy under contract number DE-AC02-76SF00515. PHB, EG, EI, and DAR were supported by the U.S. Department of Energy, Office of Science, Office of Fusion Energy Sciences under award DE-SC0020076. GS would like to acknowledge support from the EPSRC (grant numbers: EP/P010059/1, EP/T021659/1, and EP/V044397/1).

## Appendix A. Dark Current Calibration

To estimate the number of electrons at each accelerator dark current shot, Gafchromic EBT3 Radiochromic films were used [36]. The RCF films were placed in front of the Cherenkov calorimeter detector and the absorbed dose in the films was recorded for two define time periods, 3270 s and 650 s.

The RCFs were digitized using a commercial scanner model Epson Perfection V750 Pro [37]. The chosen flatbed scanner allows to store information of 16-bit RGB color information from the scanned film. By calibrating the scanner transmission light, one can retrieve the optical density of the irradiated RCFs by using the digitized color counts for each individual RGB channel. From the optical density, information retrieved from the RCFs, the absorbed dose is obtained [38]. The total number of electrons that have passed through a selected area of an RCF is given by [38]

$$N_e = \frac{d\rho}{e E_{abs}} A_p \sum_{i,j} [D(C_R)_{i,j} - D_{bkg}] , \quad (\text{A.1})$$

where  $D_{bkg}$  is the average background dose noise on the RCF,  $e$  is the electron charge,  $d = 28 \mu\text{m}$  and  $\rho = 1.20 \text{ g/cm}^3$  are the thickness and density of the active layer of the

radiochromic film,  $A_p = (25.4 \text{ mm}/300)^2$  is the area for one pixel, and,  $D(C_R)_{i,j}$  is the total absorbed dose at the pixel given by the indexes  $(i, j)$ .

The dark current of the accelerator is considered as a constant background source or noise on the measurements and has a frequency of 260 MHz. At the charge calibration measurements, the noise given by the dark current needs to be taken into account. The dark current can be measured as soon as the radio frequency (RF) injector gun was activated by opening the accelerator shutter. The total number of dark current electrons can be calculated using the following equation,

$$N_e^{dc} = N_e^c \times 260 \text{ MHz} \times T, \quad (\text{A.2})$$

where  $T$  is the total RCF exposure time to the dark current,  $N_e^c$  is the average number of electrons in one dark current cycle. The RCF used for the dark current measurement is shown in Fig. A1.

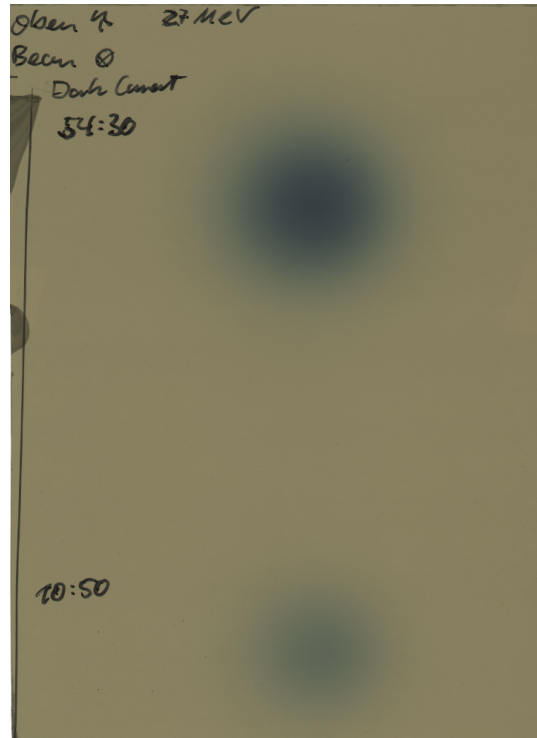


**Figure A1.** Radiochromic film used for determining the dark current of the ELBE accelerator.

By scanning the RCF shown in Fig. A1 with the Epson Perfection V750 Pro flatbed scanner and post processing the individual color channels, the two available measurements of the dark current were analyzed. The first measurement was irradiated for a period of time of approximately 11 min and resulted on an average of 0.164 electrons per 3.846 ns, equivalently to a current of  $I_{dc}^{11} = 6.81 \text{ pA}$ . The second dark current measurement spot was irradiated for a period of 54.5 min and yield an average of 0.150 electrons per 3.846 ns, or  $I_{dc}^{54.5} = 6.23 \text{ pA}$ . The mean value between the

two measurements was set to be the dark current of the calibration experiment,  $I_{dc} = 6.52 \text{ pA}$ .

## References

- [1] Karshenboim S G, Eidelman S, Fendel P, Ivanov V, Kolachevsky N, Shelyuto V and Hänsch T 2006 *Nucl. Phys. B, Proc. Suppl.* **162** 260–263
- [2] Ritus V I 1985 *J. Sov. Laser Res.* **6** 497–617
- [3] Di Piazza A, Müller C, Hatsagortsyan K Z and Keitel C H 2012 *Rev. Mod. Phys.* **84**(3) 1177–1228
- [4] Aaboud M e a 2017 *Nat. Phys.* **13** 852–858 ISSN 1745-2473
- [5] Nielsen C F, Justesen J B, Sørensen A H, Uggerhøj U I and Holtzapple R (CERN NA63 Collaboration) 2020 *Phys. Rev. D* **102**(5) 052004
- [6] Yakimenko V, Meuren S, Del Gaudio F, Baumann C, Fedotov A, Fiuza F, Grismayer T, Hogan M J, Pukhov A, Silva L O and White G 2019 *Phys. Rev. Lett.* **122**(19) 190404
- [7] Strickland D and Mourou G 1985 *Opt. Commun.* **55** 447–449
- [8] Mourou G A, Tajima T and Bulanov S V 2006 *Rev. Mod. Phys.* **78**(2) 309–371
- [9] Lureau F, Matras G, Chalus O, Derycke C, Morbieu T, Radier C, Casagrande O, Laux S, Ricaud S, Rey G *et al.* 2020 *High Power Laser Sci. Eng.* **8**
- [10] Gies H, Karbstein F, Kohlfürst C and Seegert N 2018 *Phys. Rev. D* **97** 076002
- [11] Heinzl T, Liesfeld B, Amthor K U, Schwöerer H, Sauerbrey R and Wipf A 2006 *Opt. Commun.* **267** 318–321 ISSN 00304018
- [12] Karbstein F, Gies H, Reuter M and Zepf M 2015 *Phys. Rev. D* **92** ISSN 1550-7998
- [13] Bula C, McDonald K T, Prebys E J, Bamber C, Boege S, Kotseroglou T, Melissinos A C, Meyerhofer D D, Ragg W, Burke D L, Field R C, Horton-Smith G, Odian A C, Spencer J E, Walz D, Berridge S C, Bugg W M, Shmakov K and Weidemann A W 1996 *Phys. Rev. Lett.* **76**(17) 3116–3119
- [14] Burke D L, Field R C, Horton-Smith G, Spencer J E, Walz D, Berridge S C, Bugg W M, Shmakov K, Weidemann A W, Bula C, McDonald K T, Prebys E J, Bamber C, Boege S J, Koffas T, Kotseroglou T, Melissinos A C, Meyerhofer D D, Reis D A and Ragg W 1997 *Phys. Rev. Lett.* **79**(9) 1626–1629
- [15] Bamber C, Boege S J, Koffas T, Kotseroglou T, Melissinos A C, Meyerhofer D D, Reis D A, Ragg W, Bula C, McDonald K T, Prebys E J, Burke D L, Field R C, Horton-Smith G, Spencer J E, Walz D, Berridge S C, Bugg W M, Shmakov K and Weidemann A W 1999 *Phys. Rev. D* **60**(9) 092004
- [16] Reiss H R 1971 *Phys. Rev. Lett.* **26** 1072–1075 ISSN 0031-9007
- [17] Keitel C H, Di Piazza A, Paulus G G, Stoehliker T, Clark E L, Mangles S, Najmudin Z, Krushelnick K, Schreiber J, Borghesi M, Dromey B, Geissler M, Riley D, Sarri G and Zepf M 2010 (arXiv:2103.06059v1)
- [18] Cole J M, Behm K T, Gerstmayr E, Blackburn T G, Wood J C, Baird C D, Duff M J, Harvey C, Ilderton A, Joglekar A S, Krushelnick K, Kuschel S, Marklund M, McKenna P, Murphy C D, Poder K, Ridgers C P, Samarin G M, Sarri G, Symes D R, Thomas A G R, Warwick J, Zepf M, Najmudin Z and Mangles S P D 2018 *Phys. Rev. X* **8** 011020
- [19] Poder K, Tamburini M, Sarri G, Di Piazza A, Kuschel S, Baird C D, Behm K, Bohlen S, Cole J M, Corvan D J, Duff M, Gerstmayr E, Keitel C H, Krushelnick K, Mangles S P D, McKenna P, Murphy C D, Najmudin Z, Ridgers C P, Samarin G M, Symes D R, Thomas A G R, Warwick J and Zepf M 2018 *Phys. Rev. X* **8** 031004
- [20] Meuren S 2019 Probing strong-field QED at FACET-II (SLAC E-320) [https://conf.slac.stanford.edu/facet-2-2019/sites/facet-2-2019.conf.slac.stanford.edu/files/basic-page-docs/sfqed\\_2019.pdf](https://conf.slac.stanford.edu/facet-2-2019/sites/facet-2-2019.conf.slac.stanford.edu/files/basic-page-docs/sfqed_2019.pdf)
- [21] Meuren S 2020 E-320: Probing Strong-field QED at FACET-II [https://facet.slac.stanford.edu/sites/facet.slac.stanford.edu/files/E320\\_PAC2020\\_Meuren.pdf](https://facet.slac.stanford.edu/sites/facet.slac.stanford.edu/files/E320_PAC2020_Meuren.pdf)

- [22] Altarelli M, Assmann R, Burkart F, Heinemann B, Heinzl T, Koffas T, Maier A R, Reis D, Ringwald A and Wing M 2019 (arXiv:1905.00059v1)
- [23] Hartin A, Ringwald A and Tapia N 2019 *Phys. Rev. D* **99**(3) 036008
- [24] Abramowicz H, Altarelli M, Aßmann R, Behnke T, Benhammou Y, Borysov O, Borysova M, Brinkmann R, Burkart F, Büßer K, Davidi O, Decking W, Elkina N, Harsh H, Hartin A, Hartl I, Heinemann B, Heinzl T, TalHod N, Hoffmann M, Ilderton A, King B, Levy A, List J, Maier A R, Negodin E, Perez G, Pomerantz I, Ringwald A, Rödel C, Saimpert M, Salgado F, Sarri G, Savoray I, Teter T, Wing M and Zepf M 2019 (arXiv: 1909.00860)
- [25] Abramowicz H, Acosta U H, Altarelli M, Assmann R, Bai Z, Behnke T, Benhammou Y, Blackburn T, Boogert S, Borysov O, Borysova M, Brinkmann R, Bruschi M, Burkart F, Büßer K, Cavanagh N, Davidi O, Decking W, Dosselli U, Elkina N, Fedotov A, Firlej M, Fiutowski T, Fleck K, Gostkin M, Grojean C, Hallford J A, Harsh H, Hartin A, Heinemann B, Heinzl T, Helary L, Hoffmann M, Huang S, Huang X, Idzik M, Ilderton A, Jacobs R M, Kaempfer B, King B, Lakhno H, Levanon A, Levy A, Levy I, List J, Lohmann W, Ma T, Macleod A J, Malka V, Meloni F, Mironov A, Morandini M, Moron J, Negodin E, Perez G, Pomerantz I, Poeschl R, Prasad R, Quere F, Ringwald A, Roedel C, Rykovanov S, Salgado F, Santra A, Sarri G, Saevvert A, Sbrizzi A, Schmitt S, Schramm U, Schuwalow S, Seipt D, Shaimerdenova L, Shchedrolosiev M, Skakunov M, Soreq Y, Streeter M, Swientek K, Hod N T, Tang S, Teter T, Thoden D, Titov A, Tolbanov O, Torgrimsson G, Tyazhev A, Wing M, Zanetti M, Zarubin A, Zeil K, Zepf M and Zhemchukov A 2021 (ArXiv: 2102.02032)
- [26] 2021 ICCD camera, intensified imaging, intensified ccd camera, image intensifier <https://stanfordcomputeroptics.com/products/picosecond-iccd.html>, Accessed: 20.04.2021
- [27] Et-Enterprises 2019 *25 mm (1") Photomultiplier - 9111B series datasheet*
- [28] 2021 PicoScope 6000 - high performance USB scope <https://bit.ly/2VWxUdK>, Accessed: 09.03.2021
- [29] Agostinelli S *et al.* 2003 *Nucl. Instrum. Meth. A* **506** 250–303
- [30] Allison J *et al.* 2006 *IEEE Trans. Nucl. Sci.* **53** 270–278
- [31] Allison J *et al.* 2016 *Nucl. Instrum. Meth. A* **835** 186–225
- [32] Yakimenko V, Alsberg L, Bong E, Bouchard G, Clarke C, Emma C, Green S, Hast C, Hogan M J, Seabury J, Lipkowitz N, O’Shea B, Storey D, White G and Yocky G 2019 *Phys. Rev. Accel. Beams* **22**(10) 101301
- [33] Meuren S, Keitel C H and Di Piazza A 2016 *Phys. Rev. D* **93**(8) 085028
- [34] Fassò A, Ferrari A, Ranft J and Sala P R 2005 *CERN-2005-10 (2005), INFN/TC-05/11, SLAC-R-773*
- [35] Böhlen T, Cerutti F, Chin M, Fassò A, Ferrari A, Ortega P, Mairani A, Sala P, Smirnov G and Vlachoudis V 2014 *Nucl. Data Sheets* **120** 211–214
- [36] 2021 Gafchromic Dosimetry Media, Type EBT-3, Ashland Inc. [http://www.gafchromic.com/documents/EBT3\\_Specifications.pdf](http://www.gafchromic.com/documents/EBT3_Specifications.pdf), Accessed: 10.04.2021
- [37] 2021 User’s Guide Perfection V700 Photo/V750 Pro, Seiko Epson K.K. <https://files.support.epson.com/pdf/prv7ph/prv7phug.pdf>, Accessed: 10.04.2020
- [38] Wulff J 2020 Construction and Calibration of a Single Particle Cherenkov Calorimeter for Strong-field QED Experiments Bachelor thesis